Mechanistic Studies of Liquid Metal Anode SOFCs

I. Oxidation of Hydrogen in Chemical - Electrochemical Mode

Aliya Toleuova,[a,b,*] **William C. Maskell,**[a,c,**,z] **Vladimir Yufit,**[c,**] **Paul R. Shearing,**[a] **and Daniel J. Brett**[a,z]

[a]*Electrochemical Innovation Lab, Department of Chemical Engineering, University College London, London WC1E 7JE, United Kingdom*
[b]*School of Engineering, Nazarbayev University, Astana 010000, Kazakhstan*
[c]*Department of Earth Science and Engineering, Imperial College London, London SW7 2AZ, United Kingdom*

Liquid metal anode (LMA) solid oxide fuel cells (SOFCs) are a promising type of high temperature fuel cell suitable for the direct oxidation of gaseous or solid fuel. Depending upon the operating conditions they can be run in four different modes. In this first of a series of studies concerning the mechanism of reaction and species transport in LMA SOFCs, the oxidation of hydrogen fuel in a liquid tin anode has been investigated. An electrochemical model is developed based upon fast dissolution of hydrogen in a molten tin anode, slow, rate-determining homogeneous reaction of hydrogen with oxygen dissolved in the liquid tin, followed by anodic oxygen injection under diffusion control to replace the oxygen removed by reaction (so-called Chemical - Electrochemical mode or *CE* mode). Experimentally-generated data are used to validate the model. The model has introduced a new key parameter, $\overline{z}$, which takes a value between zero and unity; its value is determined by geometric and convective factors in the cell as well as the partial pressure of the supplied hydrogen fuel. Current output of the cell is proportional to the value of $\overline{z}$.
© 2015 The Electrochemical Society. [DOI: 10.1149/2.0391509jes] All rights reserved.

Increasing interest is being shown in solid oxide fuel cells (SOFC) with liquid metal anodes.[1–10] A key advantage of such systems is the ability to perform direct oxidation of solid carbonaceous fuel, while avoiding the need for fuel pre-gasification or pre-treatment of contaminants.[11] Ability to operate using solid fuel directly, improved anode tolerance to impurities and fuel flexibility are important advantages compared with conventional SOFCs.[12–14] The robustness of liquid metal anode SOFCs is inherently enhanced by the fact that the anode is able to act as an additional energy source (electrochemical oxidation of the anode itself), the so-called "battery" effect, which can be beneficial in case of interruption of fuel supply.[15,16]

Technological developments of these SOFC systems operating with various anode metals have been reviewed recently.[17] Pioneering studies of liquid tin anode SOFCs have been performed by Tao et al.[18] at Cell Tech Power. Subsequent investigation of alternatives to Sn (p-orbital electron metals In, Pb, Bi and Sb) has been made at the University of Pennsylvania.[3,4,6] Further characterization of alloys of some of those metals (Sn-Pb, Sn-Pb-Bi) was performed by Labarbera et al.[5] The thickness of the liquid metal anode as well as the surface roughness of electrolyte[10] are also factors that may affect the performance of LMA SOFCs, albeit beyond the scope of the current study.

The operation of the liquid metal anode solid oxide fuel cell (LMA SOFC) is shown in Figure 1. Oxygen is reduced at the cathode to oxygen ions, which migrate through the solid electrolyte to the molten metal anode. Molten metal is electrochemically oxidized to metal oxide, which is reduced back to metal via chemical reaction with fuel fed into the melt. Various gaseous or solid fuels (e.g. hydrogen or carbon in Figure 1) can be utilized, resulting in products such as water or, carbon dioxide respectively.

Possible mechanistic processes that define performance of the molten anode are shown in Figure 1. The precise mechanisms occurring and the species involved in the liquid metal media are not well documented and furthermore, they depend upon the metal and reactant used.[17]

So far, the most widely studied metal anode is tin and its alloys,[17] and is the subject of this work. The approach employed with tin is applicable to a range of molten metals (M) under investigation. Numerous studies on liquid tin anode SOFCs have established deterioration in cell performance due to the formation of a blocking

layer of SnO_2.[6,15,19–21] Therefore, it was decided to operate the liquid tin anode SOFC in conditions where an insoluble SnO_2 layer is not formed and yet the fuel oxidation may be observed. This mode of operation is applied in the present work. Prior to any discussion of the applied mode of operation, a general classification of possible modes of operation of LMA SOFC is appropriate as is summarized below.

Depending upon the reaction conditions, in an LMA SOFC four different modes of operation are proposed (Figure 2):

a) Direct electrochemical oxidation of fuel at the liquid anode / electrolyte interface – classified as *E* (Electrochemical mode).
b) Homogeneous oxidation of fuel in the bulk of the liquid anode by dissolved oxygen, followed by electrochemical injection of oxygen to replace the consumed oxygen – classified as *CE* (Chemical – Electrochemical mode).
c) Electrochemical oxidation of liquid metal at the anode/electrolyte interface, followed by chemical oxidation of fuel by metal oxide in the bulk of the metal – classified as *EC1* (Electrochemical – Chemical mode 1).
d) Electrochemical oxidation of liquid metal at a rate significantly higher than metal oxide reduction with fuel, which may lead to the formation of a blocking metal oxide layer – classified as *EC2* (Electrochemical – Chemical mode 2 - blocking). This mode is only applicable for metal oxides that are in solid phase at operating temperature.

In the first two modes (*E* and *CE*) the fuel cell is operated within a potential window in which the LMA is electrochemically inert (i.e. not oxidized by the oxide ion flux) and hence electrochemical oxidation of the fuel occurs directly at the LMA/electrolyte interface (in the case of mode *E*). However, if the concentration of dissolved oxygen in the melt is sufficient (as in the case of mode *CE*), H_2 dissolves in the liquid metal and undergoes homogeneous oxidation with dissolved oxygen, reducing the concentration of dissolved oxygen, $[O]_{Sn}$, via Reaction 1:

$$2[H]_{Sn} + [O]_{Sn} \leftrightarrows H_2O \qquad [1]$$
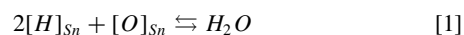
Consumption of dissolved oxygen drives the anodic generation of oxygen at the liquid tin/YSZ interface via Reaction 2:

$$O^{2-} \rightleftarrows [O]_{Sn} + 2e^- \qquad [2]$$

Due to the reported low solubility of H_2 in liquid tin[15] (0.9×10^{-4} at% $[H]_{Sn}$ at 1000°C) compared with that measured by Ramanarayanan and Rapp[22] for oxygen (0.91 at% $[O]_{Sn}$ at 1000°C) the rate of reaction
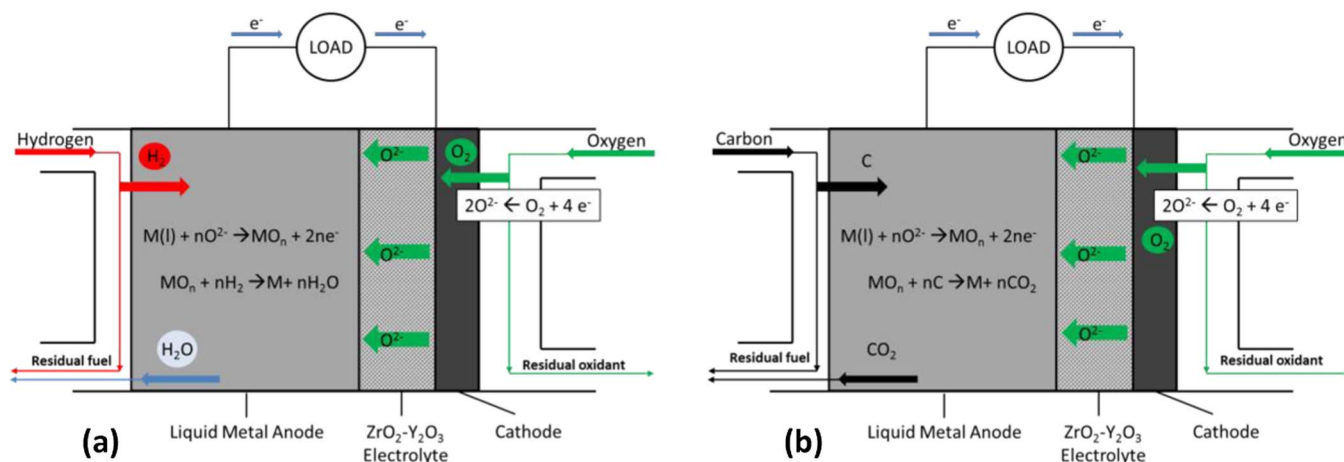
Figure 1. Schematic showing operation of LMA SOFC with (a) hydrogen and (b) solid carbon as the fuel. Yttria-stabilized zirconia (YSZ) is shown as a representative solid oxide electrolyte.
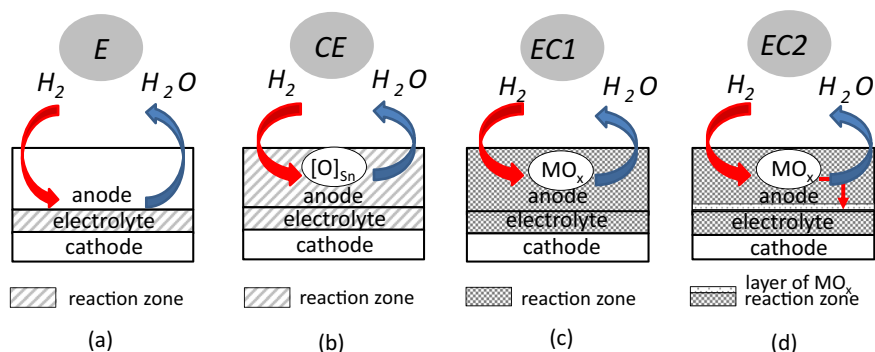

Figure 2. Proposed modes of operation for a LMA SOFC fueled with H_2: (a) direct electrochemical oxidation of H_2 at LMA/electrolyte interface; (b) chemical oxidation of H_2 in the bulk of LMA by dissolved oxygen, followed by electrochemical injection of oxygen at LMA/electolyte interface; (c) electrochemical oxidation of M followed by chemical oxidation of H_2 in the bulk of the LMA; (d) extensive oxidation of M to insoluble MO_x that may create a blocking layer.

in the **E** mode is likely to be insignificant compared with the **CE** mode. The latter mechanism (dominant **CE** mode), proposed here, entails homogeneous oxidation of hydrogen in the bulk of tin as the chemical and rate-determining process (see Figure 2b).

In **EC** modes the liquid metal is electrochemically oxidized, and then chemically reduced back to the metal via fuel oxidation, as follows:

$$M_{(l)} + nO^{2-} \leftrightarrow MO_n + 2ne^- \quad [3]$$

$$MO_n + nH_2 \leftrightarrow M + nH_2O \quad [4]$$
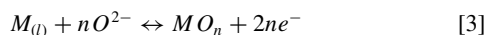
The rate of electrochemical oxidation of M is clearly greater than or equal to the rate of chemical reduction of MO_n. The ratio of the two rates is given by x:

$$x = \frac{a}{b} \geq 1 \quad [5]$$

where a is the rate of electrochemical oxidation of M to MO_n at the electrolyte interface; b is the rate of chemical reduction of MO_n to M in the bulk LMA.

In **EC1** the MO_n generated is totally reduced by fuel dissolved or present in liquid tin (i.e. $a = b$, $x = 1$). The third mode (**EC2**) is the case where the rate of electrochemical oxidation of M is greater than the rate of chemical reduction of MO_n (i.e. $a > b$, $x > 1$). During **EC2** mode there is more MO_n produced than can be readily reduced by the fuel. Taking the well-studied liquid tin anode system as an example, a layer of solid tin dioxide is accumulated at the electrolyte surface, which blocks the flow of O^{2-} ions and electrons and, as a result, inhibits further operation.[3,20,21,23] In modes **E** and **CE** there is no formation of MO_x (e.g. SnO_2) involved in the overall process, so parameter x is not relevant for these cases.

For the liquid tin anode (LTA) hydrogen-fuelled SOFC, the equilibrium potentials of the H_2-H_2O, Sn-SnO and Sn-SnO_2 couples as functions of temperature are shown in Figure 3. Equilibrium potentials were calculated based on the Gibbs free energy of each reaction (with 21% O_2 at 1 atmosphere as oxidant). Required thermodynamic data were generated using the
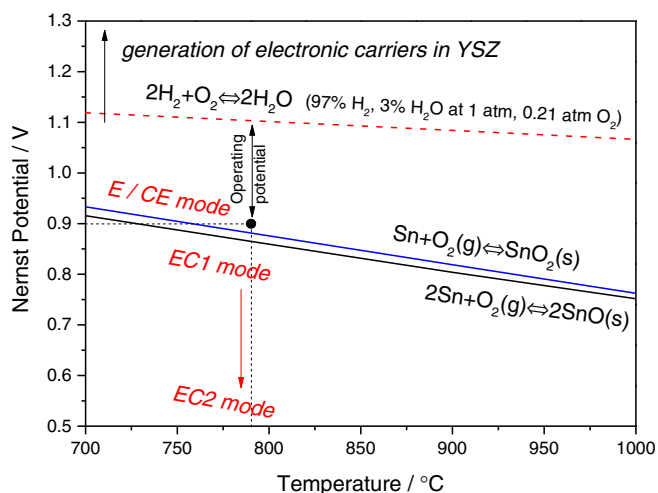

Figure 3. Equilibrium potentials of H_2-H_2O, Sn-SnO and Sn-SnO_2 redox systems (all based upon O_2 at 1 atmosphere pressure and 21% concentration) as functions of temperature. Operating potential window in E mode (applied in the present work) is constrained by the onset of electronic conductivity in YSZ from the top and by SnO_2 generation from the bottom at 780°C.

chemical reaction and equilibrium software HSC Chemistry 6.1 (Out-otec, Finland).[24]

Modes **E** and **CE** in this system can be achieved by applying a potential to the working electrode above the Sn-SnO$_2$ and Sn-SnO redox potentials. In this way, the tin anode is maintained in an effectively "inert" state and does not interfere in electrochemical reactions at the electrolyte interface. Consequently, no blocking layer of SnO$_2$ can be generated in these modes. **EC1** is initiated if the cell voltage is below the Sn-SnO$_2$ or Sn-SnO redox potential, with **EC2** becoming more likely with increasing current density/anodic overpotential (Figure 3).

Despite the remarkable advantages of LMA SOFCs there are certain technological challenges which inhibit commercialization.[17] One of the main issues is the lack of fundamental understanding of the mechanisms of reaction and transport of active species (i.e. reactants and products) within a liquid metal electrode.[15]

Development of molten anode SOFCs requires detailed investigation of the fundamentals of operation. As such, a first step toward operation on direct solid fuel is the use of a simple gaseous fuel such as hydrogen operated in **CE** mode, Figure 2. Such an approach is adopted here. Other approaches to the elucidation of anode processes in LME SOFCs include the Rotating Electrolyte Disc (RED)[25] which offers the prospect of allowing the parameters controlling mass transport of dissolved species in the melt to be studied.

Operation in mode **E** or **CE** provides a simpler system compared to other modes. It most importantly sets aside concerns with blockage of electrolyte with metal oxide.

Therefore, this paper aims to explore the dissolution of hydrogen and its subsequent oxidation in LMA SOFC. The approach used here is also applicable to other fuel gases (e.g. CO). The electrochemical model developed in this work provides a framework for the interpretation of the generated experimental data. In developing the theory, an important parameter, $\overline{z}$, is introduced which takes a value between zero and unity; the factors determining the value of $\overline{z}$ are discussed in Electrochemical model section.

Experimental

In the present paper, all experimental work entailed operation in mode **E/CE** (Figure 3). The lower potential limit of mode **E/CE** was set by the Sn-SnO$_2$ couple and the upper limit by the generation of electronic carriers in YSZ.[26] The system was operated at a constant temperature of 780°C; dry or humidified hydrogen/argon was bubbled into the tin and the working electrode was held at −0.90 V versus an air reference.

A schematic of the experimental rig used in this work is shown in Figure 4. Dry or humidified (3% water) argon (zero grade, BOC UK) was supplied to the oxygen sensor (Kent Industrial Measurements, UK) after which it was mixed with hydrogen (zero grade, BOC, UK) and supplied to the cell (Figure 5) held at operating temperature by an electric furnace (Carbolite, UK). Gases entered and exited the cell via alumina tubes with internal diameter 2 mm, the inlet tube being immersed in the liquid tin to a depth of approximately 15 mm so that the gas bubbled through the liquid tin. Gas flows were maintained at the required set point up to 100 ml per minute (1.67 ml s^{-1}) with EL-FLOW mass flow controllers (Bronkhorst UK Ltd., UK).

The working electrode (tin shots, 99.99+%, metal basis, Alfa Aesar, UK) was contained within a closed-end 8YSZ tube (McDanel Advanced Ceramic Technologies, USA). The weight of tin shots was 25 g, while the internal diameter of YSZ tube was 14 mm. Electrical connection to the working electrode (WE) was achieved using a glassy carbon rod (3 mm diameter glassy carbon rod - Sigradur HTW Hochtemperatur-Werkstoffe GmbH, Germany) immersed within the liquid tin inside the YSZ tube (Figure 5).

Platinum counter and reference electrodes (4082 Pt Vitr-Au-Less Conductor, Ferro Electronic Materials, USA) were painted on the outer side of the YSZ tube and sintered at 1000°C for 2 hours (ramp rate of 10°C per minute).

Accurate location of the reference electrode is well established for aqueous electrochemical systems and can be less trivial in the systems with thin solid electrolytes.[27] Minor errors in alignment of RE with
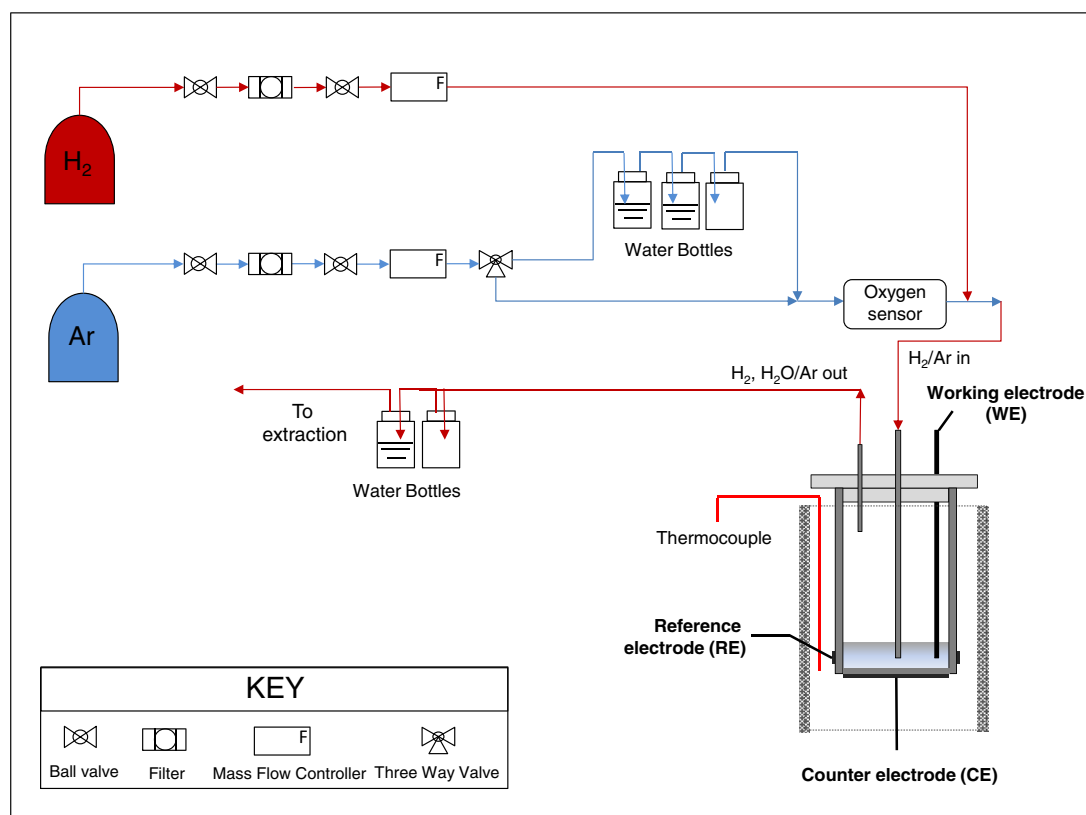

Figure 4. Process flow diagram for oxidation of hydrogen in LMA SOFC cell.
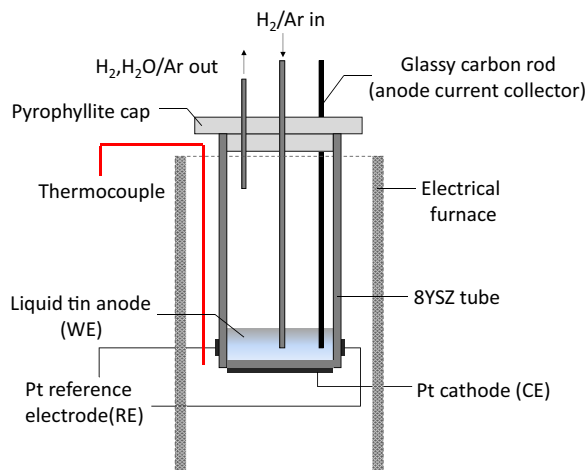
Figure 5. Schematic of an experimental setup of the LMA SOFC cell held in furnace.

Figure 6. Anodic current at −0.90 V vs. RE at 780°C (immediately after switching from 3% to zero H_2).

respect to WE can create significant errors in measurement of the working electrode[28] particularly when rapid changes in potential are involved. In the present work the geometry of symmetrical RE was similar to others used typically in the literature[29,30] whereby RE was adjacent to CE and therefore is considered to be suitable for this study.

Current collection from the cathode and reference electrode was achieved using platinum mesh and wires (Goodfellow Cambridge, UK). The total electrode (CE) area was 1.54 cm^2.

A thermocouple was placed in parallel to the tube to measure temperature separately from furnace control. A predrilled pyrophyllite cap was placed on top of the YSZ tube to hold all tubes and the glassy carbon rod in place and sealed with Silicoset 152 adhesive (ACC Silicones Ltd, UK). Electrochemical measurements were performed using an Ivium potentiostat (Ivium Technologies, Netherlands).

Results

Dissolution of hydrogen and its oxidation in LMA SOFC was investigated using the working cell operated in mode ***E/CE***. Experimental investigations were first performed to assess the effect of hydrogen partial pressure in terms of current generation and dynamics associated with changes in hydrogen concentration. These results were then used in support of an analytical modelling analysis. However, before conducting these experiments, it was necessary to assess the low levels of oxygen present in the system which cannot be totally excluded, and take account of the effect on the electrochemistry.
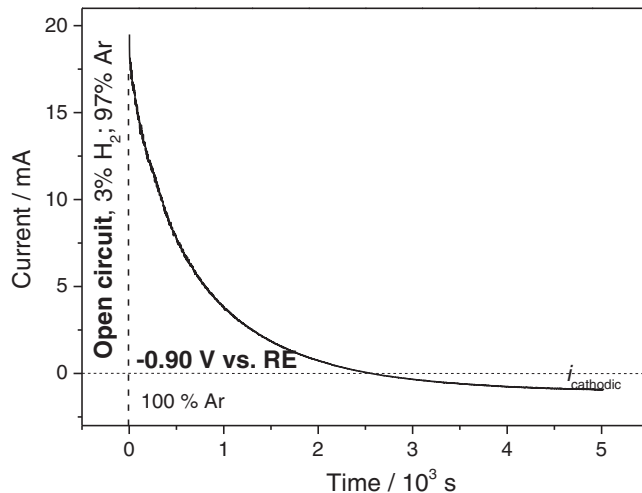
Assessment of the effect of residual oxygen.— A potentiometric oxygen sensor enabled the level of oxygen in the argon line to be monitored. In order to account for the contribution of oxygen reduction current to the overall measured current, the following procedure was performed and repeated prior to each test run in this work.

Initially, to remove residual SnO_2 present in the working cell a mixture of 3% H_2 and 97% Ar was supplied for 600–900 s. A potential of −0.90 V vs. air electrode (RE) was then applied to the working electrode while simultaneously switching the gas flow to argon with no added hydrogen (Figure 6).

The current decreased slowly to zero and then eventually to a steady negative current, $i_{cathodic}$; this negative current was due to the parasitic level of oxygen in the system (−1.0 mA in Figure 6).

The current at zero hydrogen input, $i_{cathodic}$, was measured throughout the experiments presented in this work; anodic current data were corrected in each case for the individual measured value of $i_{cathodic}$.

Oxidation of hydrogen in LTA SOFC.— Hydrogen of partial pressures from 8 to 26 kPa was supplied to the LMA at 780°C. A potential of −0.90 V vs. air electrode (RE) was applied. The anodic current was monitored with time while $p(H_2)$ was increased step-wise from zero to 8, 15 and 26 kPa (Figure 7a) and likewise was reduced from 26 kPa to zero (Figure 7b).

The same procedure was repeated, varying the total flow rate while maintaining a constant $p(H_2)$, as shown in Figure 8.

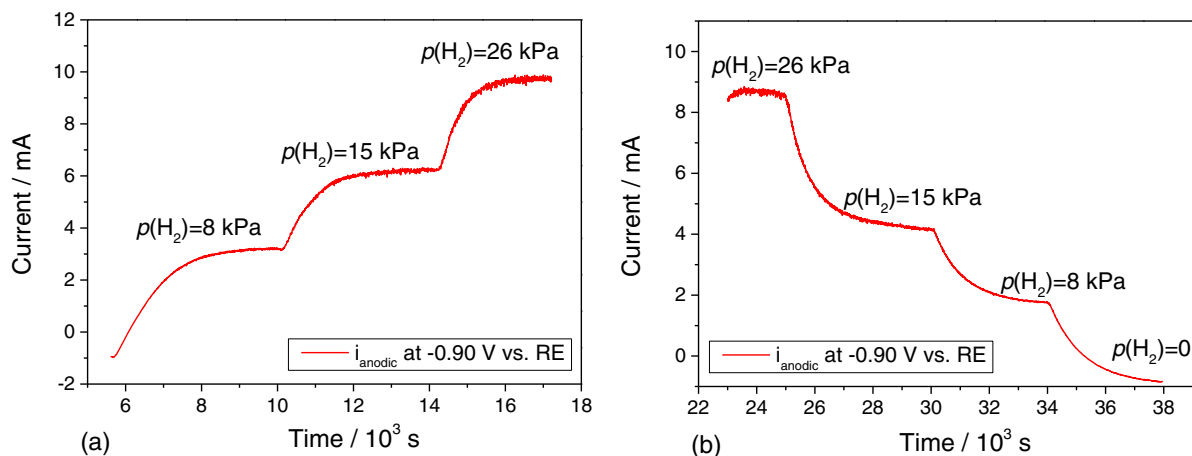**Figure 7.** Anodic current at −0.90 V vs. RE at 780°C with increase of $p(H_2)$ from 0 to 26 kPa (a); and with decrease of $p(H_2)$ from 26 kPa to 0 (b).
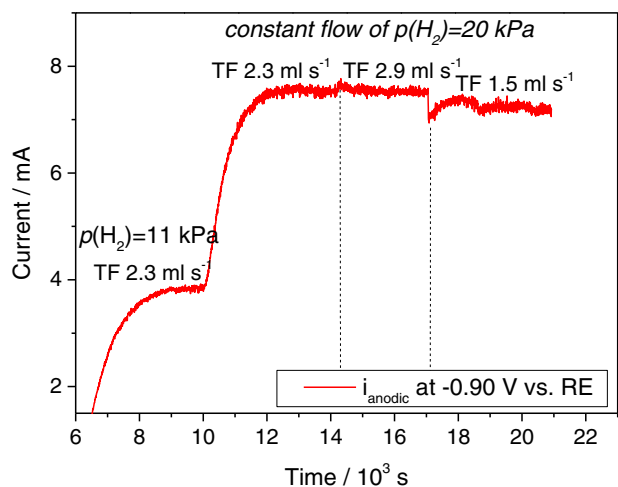
Figure 8. Anodic current with variation of $p(H_2)$ and of total flow rate (TF) at 780°C.

The results in Figure 8 confirm that changes in total flow rate (shown as TF in Figure 8) had only a minimal effect on the measured steady anodic current.

Steady anodic currents as a function of $p(H_2)$ with various total flow rates and direction of $p(H_2)$ modulation are summarized in Figure 9. The currents shown have been corrected for parasitic oxygen reduction current, $i_{cathodic}$ (see Assessment of the effect of residual oxygen section).

Proportionality between steady oxidation current and H_2 partial pressure with no hysteresis and no significant sensitivity to total flow rate was evident (for the range of flow rates studied, 1.5 – 3.2 ml s^{-1}). Further refinement of the analysis is performed in Experimental validation of model section.

Theory and Model Development

Introduction.— The following electrochemical models were developed as a step toward a better understanding of the performance of solid oxide fuel cells with liquid metal anodes. Modelling of the cell operating either in mode *E,* involving direct anodic oxidation of dissolved hydrogen, or in mode *CE* on a basis of dissolution and homogeneous oxidation of hydrogen as well as replacement of dis-
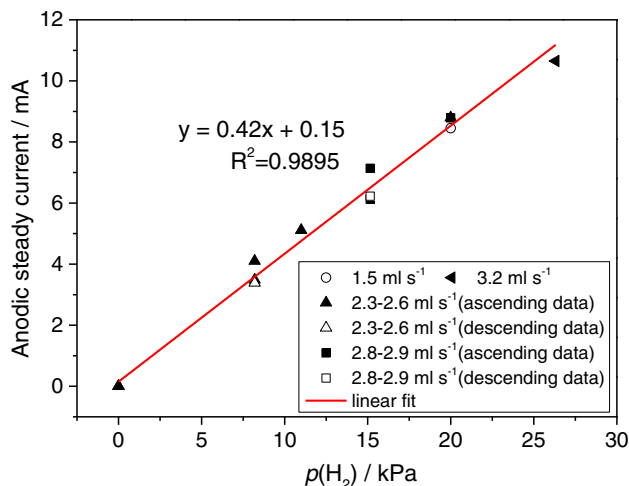

Figure 9. Steady anodic oxidation current as function of $p(H_2)$ with varying TF and direction of change of H_2 composition (ascending/descending), all at 780°C.

solved oxygen by anodic generation, is the primary focus of this paper. Additional descriptions and analysis of operation in *EC* modes will be covered in the subsequent papers in this series. The model developed is anticipated to generate essential parameters required for composing numerical models suitable for the development of technological systems. The models provide a framework for the analysis and interpretation of data obtained, as described in the previous section.

Model development and experimental validation.— Electrochemical model.— Initial results, shown in Figures 7–9, demonstrate three significant points:

i)   steady anodic currents were proportional to hydrogen partial pressure (this is refined later in the paper);
ii) steady anodic currents were essentially independent of total gas flow rate;
iii) following step changes in hydrogen partial pressure, the current-time behavior displayed a gradual and progressive change between the two endpoints, which appeared to be exponential in character.

Two models were developed and tested against the experimental data.

The first model was based upon incorporation of hydrogen into the tin according to Henry's law, followed by its diffusion to the interface and anodic oxidation. The model required that the tin and bubbled gases form a persistent foam effectively 'storing' hydrogen which would then be available for electrochemical oxidation An investigation aimed at the detection of a foam above the liquid tin was undertaken but yielded a negative result. Thus model *E* (direct anodic oxidation of hydrogen) in LMA SOFC is not applicable to this system.

The second was an electrochemical model (type *CE*) involving fast dissolution of hydrogen in liquid tin according to Sievert's law[31–34] followed by slow (rate-determining) reaction with oxygen dissolved in liquid tin similarly governed by Sievert's law:[35] the observed anodic current is then driven by the reduction in dissolved oxygen concentration in the melt, resulting in injection of oxygen via the YSZ- tin interface to replace the oxygen consumed in the chemical reaction.

The chemical reaction is shown earlier as 1:

$$2[H]_{Sn} + [O]_{Sn} \rightleftarrows H_2O$$

The anodic reaction is shown earlier as 2:

$$[O^{2-}]_{YSZ} \leftrightarrows [O]_{Sn} + 2e^-$$
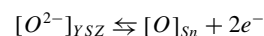
The oxygen injected diffuses into the bulk of the tin from the interface.

The assumptions made are as follows:

i)   The electrochemical kinetics of the electrode reaction are fast so that the concentration of dissolved oxygen at the YSZ-tin interface is fixed by the applied potential and is not disturbed by the current flow.
ii) The concentration of dissolved hydrogen in liquid tin is the saturated concentration appropriate to the partial pressure of the hydrogen supplied (bubbled) as a gas and obeys Sievert's law.
iii) The rate of homogeneous oxidation of hydrogen by dissolved oxygen is the rate-determining step and is governed by a rate equation which is first-order with respect to monatomic oxygen.
iv) Diffusion of oxygen away from the YSZ-tin interface to replace that removed by reaction with hydrogen occurs through a diffusion layer of constant thickness as a result of convection induced by bubbling and thermal effects.
v)   The system is considered to be in quasi-equilibrium.

Consider the following: hydrogen is bubbled through the liquid tin at partial pressure p_1', a potential, E, is applied to the Sn/YSZ interface and eventually a steady current, i_1, is observed. The partial pressure of H_2 is then increased to p_2' and the current, i, increases with time and eventually stabilizes at i_2 (Figure 10). Oxygen concentrations within the liquid tin are described schematically in Figure 11.
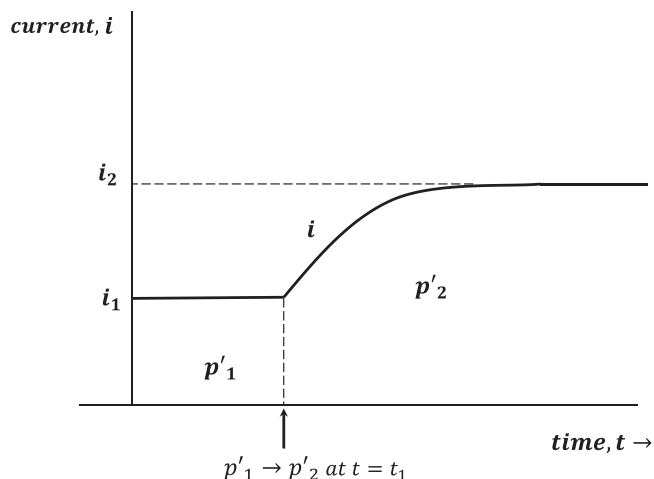
Figure 10. Schematic showing the step change in $p(\text{H}_2)$ which results in additional anodic injection of oxygen at a given applied potential in the *CE* mode of operation.

In the theoretical treatment, hydrogen concentration is denoted by a single prime and oxygen concentration is denoted by a bar.

The rate of removal of oxygen via Reaction 1 is $V k_1 \bar{c}(c')^2$, (i.e. $k_1 \bar{c}(c')^2$ per unit volume of tin) where k_1 is the rate constant for the reaction and V is the volume of tin.

The rate of injection of oxygen via Reaction 2 is i/nF ($n = 2$). Thus the net rate of removal of oxygen via the two reactions is $V k_1 \bar{c}(c')^2 - i/nF$. The concentration of hydrogen, c', for given hydrogen partial pressure, p', is given by (according to Sievert's law):

$$c' = k_2 \left(p'\right)^{1/2} \qquad [6]$$

where k_2 is a constant for a given temperature (Sievert's constant).

Expressing the total amount (gram atoms) of [O] in tin as $\bar{N}$, it follows that

$$\frac{d\bar{N}}{dt} = -V k_1 (k_2)^2 \bar{c} p' + \frac{i}{nF} \qquad [7]$$

Applying Fick's first law to the diffusion of [O] from the interface, the flux, $\bar{J}$, is given by:

$$\bar{J} = -\bar{D} A \frac{d\bar{c}}{dx} \qquad [8]$$

where $\bar{D}$ is the diffusion coefficient, A is the area of the interface and $\frac{d\bar{c}}{dx}$ is the concentration gradient within the diffusion layer. So
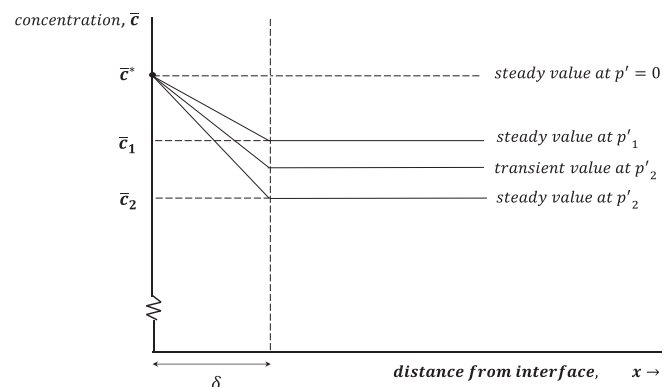

Figure 11. Schematic of the dissolved oxygen concentration profile at a given applied potential in the *CE* mode of operation. The diffusion layer thickness is shown as δ.

Equation 8 becomes (see Figure 11):

$$\bar{J} = -\bar{D} A \left(\frac{\bar{c} - \bar{c}^*}{\delta} \right) \qquad [9]$$

Equating the flux with current via Faraday's law:

$$\bar{J} = \frac{i}{nF} \qquad [10]$$

Eliminating $\bar{J}$ between 9 and 10:

$$i = \frac{nF \bar{D} A}{\delta} \left(\bar{c}^* - \bar{c} \right) \qquad [11]$$

This will be written as:

$$i = k_3 \left(\bar{c}^* - \bar{c} \right) \qquad [12]$$

where k_3 is given by:

$$k_3 = \frac{nF \bar{D} A}{\delta} \qquad [13]$$

In the steady-state situation, when $p' = p_2'$, $\bar{c} = \bar{c}_2$, $i = i_2$ and $\frac{d\bar{N}}{dt} = 0$.

So using Equation 7:

$$V k_1 (k_2)^2 \bar{c}_2 \, p_2' = \frac{i_2}{nF} \qquad [14]$$

And from 12

$$i_2 = k_3 (\bar{c}^* - \bar{c}_2) \qquad [15]$$

Eliminating i_2 between 14 and 15:

$$V k_1 (k_2)^2 \bar{c}_2 \, p_2' = \frac{k_3 \left(\bar{c}^* - \bar{c}_2 \right)}{nF}$$

So

$$\bar{c}_2 = \frac{\bar{c}^*}{1 + \frac{V k_1 (k_2)^2 p_2' nF}{k_3}}$$

Or

$$\bar{c}_2 = \bar{c}^* \left(1 + \frac{V k_1 (k_2)^2 p_2' nF}{k_3} \right)^{-1} \qquad [16]$$

Writing

$$\bar{z}_2 = \left(1 + \frac{V k_1 (k_2)^2 p_2' nF}{k_3} \right)^{-1} \qquad [17]$$

Then

$$\bar{c}_2 = \bar{z}_2 \bar{c}^* \qquad [18]$$

Note that $\bar{z}$ is a function of p' and $\bar{z} \le 1$. Likewise:

$$\bar{c}_1 = \bar{z}_1 \bar{c}^* \qquad [19]$$

We may write:

$$\frac{d\bar{c}}{dt} = \frac{1}{V} \frac{d\bar{N}}{dt} \qquad [20]$$

Eliminating i between 7 and 12 for $p' = p_2'$

$$\frac{d\bar{N}}{dt} = -V k_1 (k_2)^2 \bar{c} p_2' + \frac{k_3 \left(\bar{c}^* - \bar{c} \right)}{nF} \qquad [21]$$

From 20 and 21:

$$\frac{d\bar{c}}{dt} = \frac{1}{V} \left[-\bar{c} \left(V k_1 (k_2)^2 p_2' + \frac{k_3}{nF} \right) + \frac{k_3}{nF} \bar{c}^* \right] \qquad [22]$$

$$= \frac{k_3}{V nF} \left[-\bar{c} \left(\frac{nF V k_1 (k_2)^2 p_2'}{k_3} + 1 \right) + \bar{c}^* \right] \qquad [23]$$
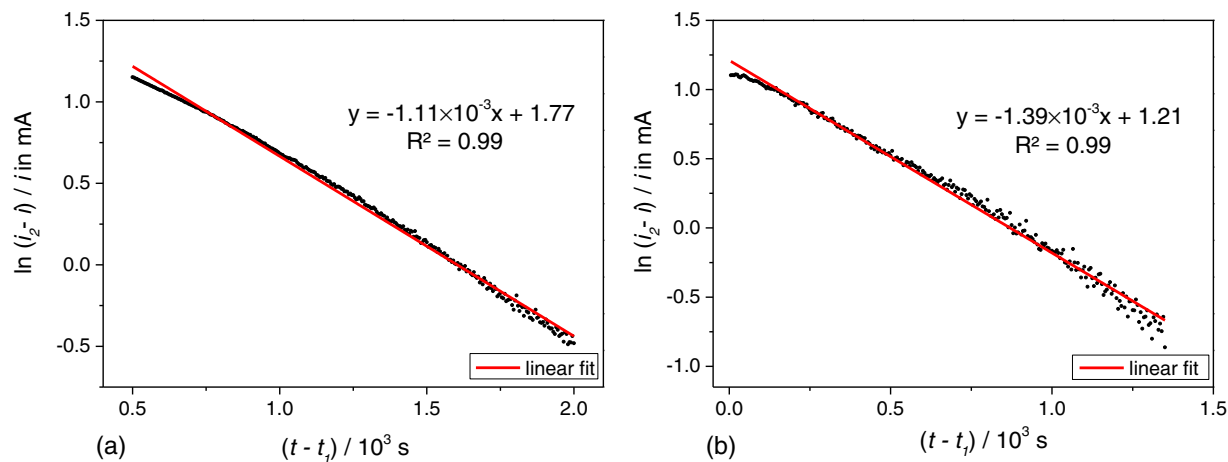
Figure 12. Step change in hydrogen partial pressure: from 0 to 8 kPa (total flow rate 2.6 ml s^{-1}) (a); from 8 to 15 kPa (total flow rate 2.8 ml s^{-1}) (b).

Then using Equation 17

$$\frac{d\bar{c}}{dt} = \frac{k_3}{VnF\bar{z}_2}\left(-\bar{c}+\bar{z}_2\bar{c}^*\right) \qquad [24]$$

Followed by 18:

$$\frac{d\bar{c}}{dt} = \frac{k_3}{VnF\bar{z}_2}\left(\bar{c}_2-\bar{c}\right) \qquad [25]$$

Integrating:

$$\int_{\bar{c}_1}^{\bar{c}} \frac{d\bar{c}}{(\bar{c}_2-\bar{c})} = \frac{k_3}{VnF\bar{z}_2}\int_{t_1}^{t} dt \qquad [26]$$

$$-ln\left[\bar{c}_2-\bar{c}\right]_{\bar{c}_1}^{\bar{c}} = \frac{k_3}{VnF\bar{z}_2}\left(t-t_1\right) \qquad [27]$$

$$ln\frac{\bar{c}_2-\bar{c}}{\bar{c}_2-\bar{c}_1} = -\frac{k_3}{VnF\bar{z}_2}(t-t_1) \qquad [28]$$

It follows from 12 and 28 that

$$ln\frac{i_2-i}{i_2-i_1} = -\frac{k_3}{VnF\bar{z}_2}(t-t_1) \qquad [29]$$

This is the required equation.

The theory allows prediction of the behavior of the system as follows:

A) From 14 and 18:

$$i_2 = nFVk_1(k_2)^2\bar{z}_2\bar{c}^*p_2' \qquad [30]$$

This shows that steady current is proportional to $\bar{z}_2 p_2'$ (rather than p_2' only, as indicated earlier) where $\bar{z}_2$ is given by 17.

B) Equation 29 indicates that a plot of $ln(i_2-i)$ for $i_2 > i_1$ [or $ln(i-i_2)$ for $i_1 > i_2$] versus time should show a straight line of slope $-\frac{k_3}{VnF\bar{z}_2}$. As $\bar{z}_2$ is a function of p_2' the slope is expected to vary with hydrogen partial pressure.

The significance of the parameter $\bar{z}$ is now briefly considered. Clearly, Equation 17 shows that $\bar{z}$ must take a value between zero and unity but its actual value in a given cell depends upon certain characteristics of the system as follows. At a given temperature $\bar{z}$ is dependent upon geometric factors (V and A) via Equations 13 and 17) and the degree of convection (related to δ which decreases with increasing convection) via Equation 13. The larger the value of k_3 (i.e. large A; small δ) then $\bar{z}$ tends toward unity; conversely, the smaller the value of k_3 (i.e. small A; large δ) then $\bar{z}$ tends toward small values with a limiting value of zero. The value of $\bar{z}$ determines the output current of the cell as shown in Equation 30.

Experimental validation of model.—Application of Equation 29 to experimental data for oxidation of hydrogen and injection of oxygen anodically at −0.90 V vs. RE at 780°C (shown in Figure 7) resulted in reasonable straight lines ($R^2_{average} > 0.98$) (Figures 12–14). The slopes obtained from Figures 12 –14 are summarized in Table I.
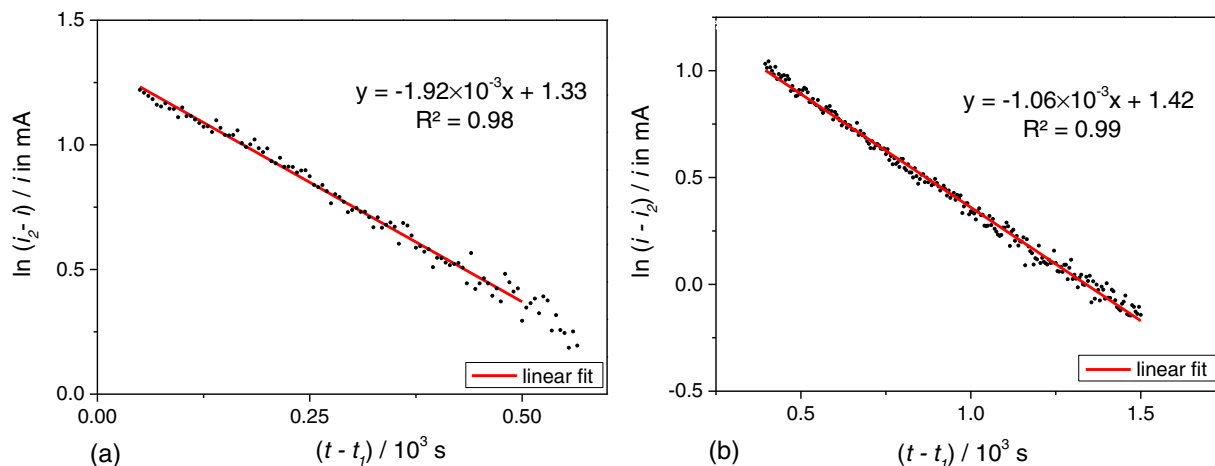

Figure 13. Step change in hydrogen partial pressure: from 15 to 26 kPa (total flow rate 3.2 ml s^{-1}) (a); from 26 to 15 kPa (total flow rate 2.8 ml s^{-1}) (b).
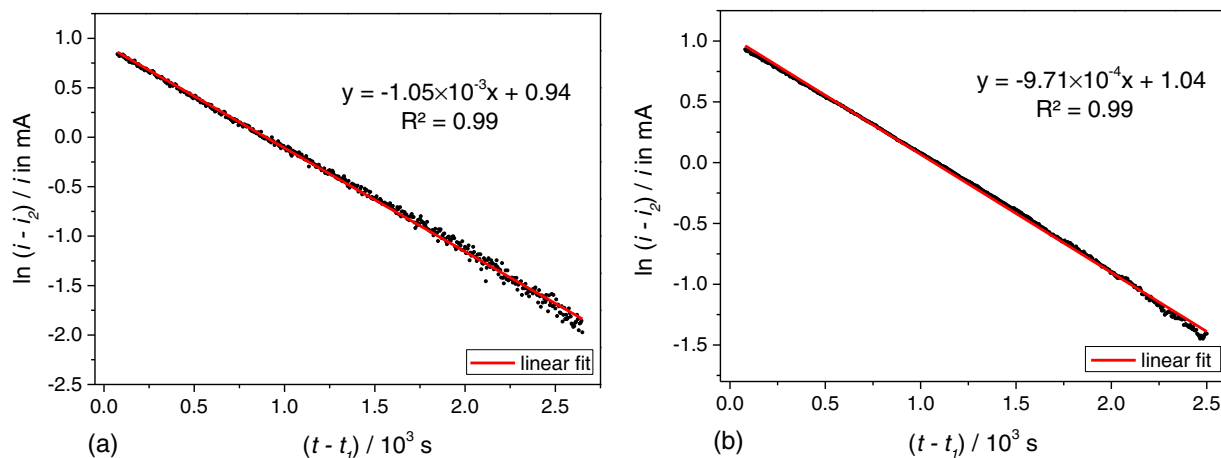
Figure 14. Step change in hydrogen partial pressure: from 15 to 8 kPa (total flow rate 2.6 ml s^{-1}) (a); from 8 kPa to 0 (total flow rate 2.3 ml s^{-1}) (b).

Table I. Reciprocal time constants for various p_2' values.

p_2'/kPa	0	8	15	26
Slope/10^{-3} s^{-1}	0.97	1.11	1.39	1.92
		1.05	1.06	
Average slope/10^{-3} s^{-1}	0.97	1.08	1.22	1.92
Time constant/s	1031	926	820	521

It is notable that the time constants (reciprocal of the slopes in Figures 12–14) for step changes in hydrogen partial pressure show a decrease with increasing $p(H_2)$ (as $\bar{z}_2$ decreases) as expected from 29 and 17. Slopes (reciprocal time constants) vs. p_2' are shown in Figure 15.

Equation 30 predicts proportionality between steady current and $\bar{z}_2 p_2'$. But $\bar{z}_2$ is itself a function of p_2' (according to 17) and hence a plot of i_2 vs. p_2' should show deviation from a straight line. Clearly, for the range of p_2' values employed in the measurements (Figure 9) the deviation is small.

Equation 17 may be written:

$$\bar{z}_2 = \left(1 + \bar{K} p_2'\right)^{-1} \quad [31]$$

where

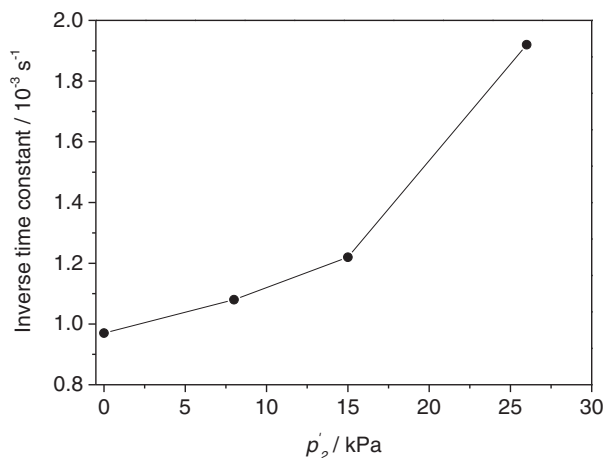$$\bar{K} = \frac{V k_1 (k_2)^2 n F}{k_3} \quad [32]$$

Figure 15. The reciprocal time constant versus p_2'.

Differentiating Equation 30 with respect to p_2':

$$\frac{di_2}{dp_2'} = nFVk_1 (k_2)^2 \bar{c}^* \frac{d}{dp_2'} \left(\bar{z}_2 p_2'\right) \quad [33]$$

leads to

$$\frac{di_2}{dp_2'} = nFVk_1 (k_2)^2 \bar{c}^* \left(1 + \bar{K} p_2'\right)^{-2} \quad [34]$$

Therefore for $p_2' = 0$ (i.e. at the origin):

$$\left(\frac{di_2}{dp_2'}\right)_{p_2' = 0} = nFVk_1 (k_2)^2 \bar{c}^* \quad [35]$$

Furthermore, differentiating 30 with respect to $\bar{z}_2 p_2'$:

$$\frac{di_2}{d\left(\bar{z}_2 p_2'\right)} = nFVk_1 (k_2)^2 \bar{c}^* \quad [36]$$

So comparing 35 and 36 it follows that

$$\left(\frac{di_2}{dp_2'}\right)_{p_2' = 0} = \frac{di_2}{d\left(\bar{z}_2 p_2'\right)} = nFVk_1 (k_2)^2 \bar{c}^* \quad [37]$$

where $\bar{z}_2$ is given by 31.

So Equation 37 shows that the slope of the tangent to the curve of i_2 versus p_2' at the origin is $nFVk_1(k_2)^2\bar{c}^*$ which is identical to the slope of the straight line plot of i_2 versus $\bar{z}_2 p_2'$.

The difficulty of applying Equation 37 to find the value of $nFVk_1(k_2)^2\bar{c}^*$, which is required in Experimental validation of additional mechanistic theory section for validation of the model, is that $\bar{z}_2$ is not known as a function of p_2' except at $p_2' = 0$ where $\bar{z}_2 =$ unity (i.e. the value of $\bar{K}$ in Equation 31 is not known). So the following procedure was adopted to address this problem.

- A value for $\bar{K}$ was assumed.
- Using this value of $\bar{K}$ together with the data in Figure 9, i_2 was plotted versus $\bar{z}_2 p_2'$.
- The best line through the data points was determined by a linear regression analysis which provided the slope of the line, the intercept at $p_2' = 0$ and the R-squared value. The last-mentioned is a measure of the goodness of fit of the data to a straight line.
- The above was repeated for other values of $\bar{K}$, and then the slope, intercept and R-squared values were plotted versus $\bar{K}$.
- The $\bar{K}$ value, which provided the value for R-squared closest to unity, was determined from the plots and this was denoted $\bar{K}_{best}$.
- $\bar{K}_{best}$ is the most likely value of $\bar{K}$. It is however not possible to put an uncertainty on its value based upon any well-defined criterion. As a result, the range of possible values of the parameter was set
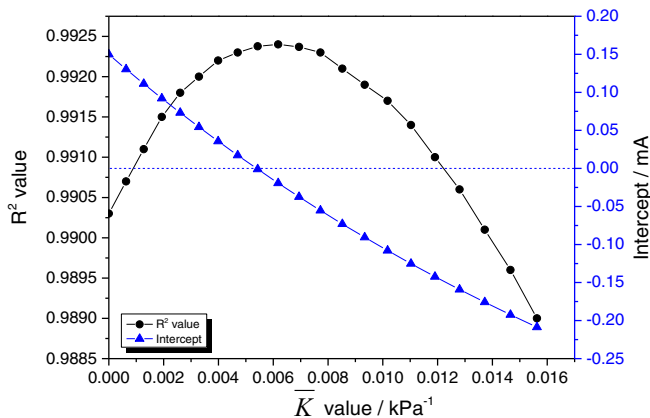
Figure 16. Determined values of R^2 and intercept for the plots of i_2 versus $\bar{z}_2 p'_2$ versus $\bar{K}$ for a range of values.

in a somewhat arbitrary way by selecting a value of R-squared less than the maximum value which then set a range of $\bar{K}$ values; by appropriate choice of the R-squared value it was ensured that this range was substantial so as to have reasonable confidence that the range encompassed the true value of $\bar{K}$. The endpoints of the range were designated $\bar{K}_{max}$ and $\bar{K}_{min}$.

• A value of $nFVk_1(k_2)^2\bar{c}^*$ together with its likely range was calculated using the determined slopes of the plots of i_2 versus $\bar{z}_2 p'_2$ at the $\bar{K}$ values given by $\bar{K}_{best}$, $\bar{K}_{max}$ and $\bar{K}_{min}$.

Results generated by applying the above procedure are shown in Figures 16–17.

The value of R-squared chosen to provide an appropriate range of $\bar{K}$ was 0.9903. This gave values for $\bar{K}_{max}$ and $\bar{K}_{min}$ of 0.014 and 0.000 respectively, resulting in $\bar{K} = 0.007 \pm 0.007$. Furthermore, at $\bar{K} = 0.007$ the intercept (Figure 16) is close to zero providing additional confidence that this best value of $\bar{K}$ is not greatly different from the true value. The slope from Figure 17 for $\bar{K} = 0.007 \pm 0.007$ is 0.48 $\pm$ 0.06 mA kPa^{-1} which is the required value for $nFVk_1(k_2)^2\bar{c}^*$; this value is applied in Experimental validation of additional mechanistic theory section for validation of the model.

Using the values for $\bar{K} = 0.007 \pm 0.007$ together with equations 30 and 31 the resulting computed curves for i_2 versus p'_2 are shown together with the original experimental data in Figure 18.
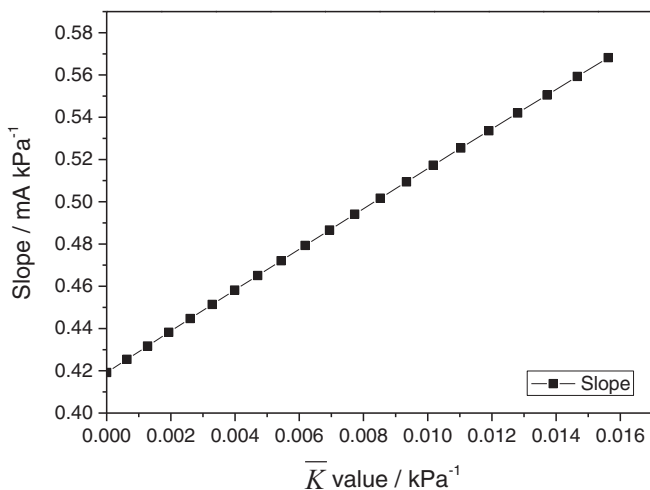

Figure 17. Determined values for the slope of plots of i_2 versus $\bar{z}_2 p'_2$ plotted as a function of $\bar{K}$.
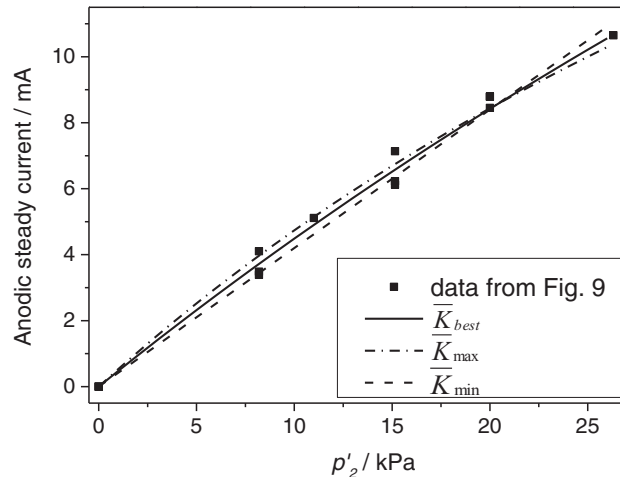

Figure 18. The 'refined' plot: steady anodic current versus p'_2. Compare Figure 9.

Additional Mechanistic Theory

A further case is now considered where the inert gas, Ar, is first bubbled through the tin for sufficient time to reduce the hydrogen concentration to a value close to zero. Then, while holding the potential at a constant value, E, a gas mixture of Ar/H$_2$ with hydrogen partial pressure p_2' is bubbled continuously, starting at time $t = t_1$, through the tin and the anodic current (due to injection of oxygen to replace that consumed by hydrogen) is measured as a function of time.

At $t = t_1$, $\bar{c} = \bar{c}^*$ and thus $i = 0$ (see Equation 12)

Equation 7 becomes

$$\left[\frac{d\bar{N}}{dt}\right]_{t=t_1} = -Vk_1(k_2)^2\bar{c}^*p'_2 \qquad [38]$$

Differentiating Equation 12

$$\left[\frac{di}{dt}\right]_{t=t_1} = -k_3\frac{d\bar{c}}{dt} \qquad [39]$$

From 20, 38 and 39:

$$\left[\frac{di}{dt}\right]_{t=t_1} = k_1(k_2)^2k_3\bar{c}^*p'_2 \qquad [40]$$

Alternatively, a similar equation may be derived as follows:

Equation 29 becomes

$$ln\left(1 - \frac{i}{i_2}\right) = -\frac{k_3}{VnF\bar{z}_2}(t - t_1) \qquad [41]$$

as $p'_1 = 0$ and $i_1 = 0$ at $t = t_1$. For $\frac{i}{i_2} \ll 1$ the logarithm linearizes as follows:

$$ln\left(1 - \frac{i}{i_2}\right) \cong -\frac{i}{i_2} \qquad [42]$$

So

$$\frac{i}{i_2} \cong \frac{k_3}{VnF\bar{z}_2}(t - t_1) \qquad [43]$$

Differentiating and combining with 30

$$\left[\frac{di}{dt}\right]_{\frac{i}{i_2}\ll 1} \cong k_1(k_2)^2k_3\bar{c}^*p'_2 \qquad [44]$$

Thus

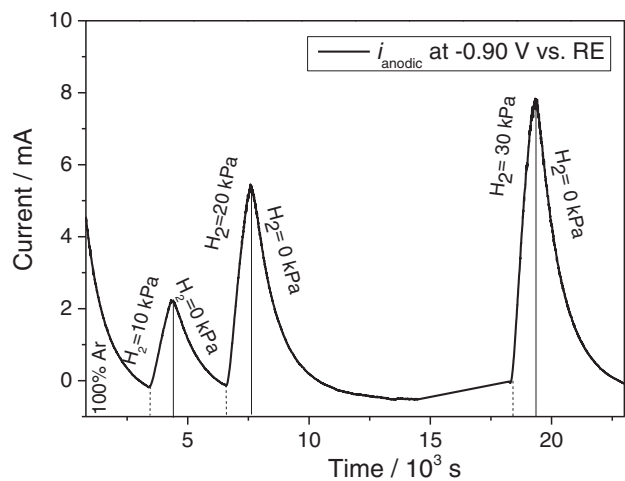$$\left[\frac{di}{dt}\right]_{\frac{i}{i_2}\ll 1} \cong \left[\frac{di}{dt}\right]_{t=t_1} \qquad [45]$$

Figure 19. Anodic current versus time in LTA SOFC at 780 °C with instantaneous step change of $p(H_2)$ from 0 to 10 kPa, then to back to zero, repeated with 20 kPa and 30 kPa.

Equation 42 is a fair approximation for i/i_2 values up to 0.2. Thus a plot of i versus t is expected to show a straight line for values of current up to at least one fifth of the steady current for a given hydrogen partial pressure.

Equations 40 and 45 predict that $\left[\frac{di}{dt}\right]_{t=t_1}$ or $\left[\frac{di}{dt}\right]_{\frac{i}{i_2}\ll 1}$ should be proportional to p_2'; a plot of $\left[\frac{di}{dt}\right]_{t=t_1}$ vs. p_2' is expected to reveal a slope of $k_1(k_2)^2 k_3 \bar{c}^*$, which will be denoted as s_1.

Equation 30 indicates that a plot of i_2 vs. $\bar{z}_2 p_2'$ has a slope of $nFVk_1(k_2)^2\bar{c}^*$, which will be denoted as s_2. It follows that:

$$\frac{s_1}{s_2} = \frac{k_3}{VnF} \qquad [46]$$

Thus the magnitude of $\frac{k_3}{VnF}$ from Equation 46 can be compared to the reciprocal time constant determined from the slopes of plots of $ln(i_2-i)$ vs. t [or $ln(i-i_2)$ vs. t] at $p_2' = 0$ (see Equation 29).

Experimental validation of additional mechanistic theory.— In order to validate this extension of the theory, the cell was first flushed with a mixture of H_2/Ar to remove any residual SnO_2, followed by Ar only while the tin electrode was held at -0.90 V vs. RE at 780°C; the ongoing parasitic leak of oxygen inevitably occurring was measured using the technique described in Assessment of the effect of residual oxygen section. The $p(H_2)$ was then stepped from zero to 10 kPa and back to zero; from zero to 20 kPa and back to zero and finally from zero to 30 kPa and back to zero. The current response was monitored with time (Figure 19).

The following current – time curves (Figures 20a–20c) were extracted from the data in Figure 19. Anodic current immediately after the switch of the hydrogen from zero to a particular partial pressure (10, 20 and 30 kPa) is shown versus time.

All three current–time curves resulted in straight lines ($R^2 > 0.98$), the slopes (di/dt) of which were then plotted against hydrogen partial pressure (Figure 20; Equation 40). It should be noted that the straight line in Figure 20d is based upon only 3 points but that each point is determined using a substantial data set; furthermore, as predicted the intercept is small (-0.18×10^{-3} mA s^{-1}) indicating direct proportionality between di/dt and p_2'.
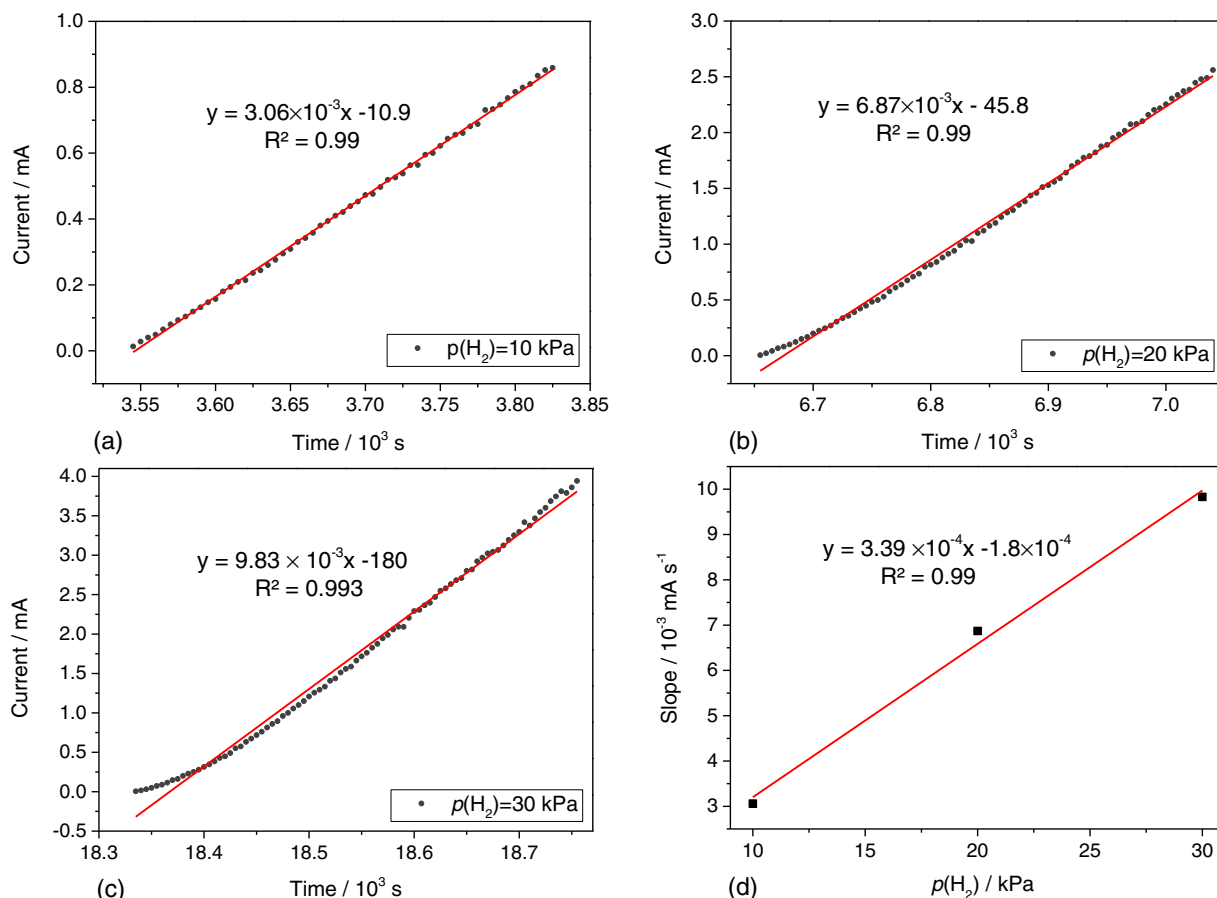

Figure 20. Current-time curves after switching the hydrogen partial pressure from 0 to 10 kPa (a); 20 kPa (b); 30 kPa (c). Slopes of the lines in (a-c) vs. $p(H_2)$ are shown in (d).

The data are interpreted using Equations 40 and 45:

$$s_1 = k_1\,(k_2)^2 k_3\,\bar{c}^* = 3.4 \times 10^{-4}\ mA\ s^{-1}\ kPa^{-1}$$

It is shown in Experimental validation of Model section that

$$s_2 = nFVk_1(k_2)^2\,\bar{c}^* = 0.48 \pm 0.06\ \text{mA kPa}^{-1}$$

Thus applying 46:

$$\frac{s_1}{s_2} = \frac{k_3}{VnF} = \frac{3.4 \times 10^{-4}}{0.48 \pm 0.06} = (0.71 \pm 0.09) \times 10^{-3}\ \text{s}^{-1}$$

This value may be compared with the value of the reciprocal time constant at $p'_2 = 0$ ($\bar{z}_2 = 1$) which is $0.97 \times 10^{-3}\ \text{s}^{-1}$ (see Table I).

The similarity of the determined values for the reciprocal time constant, ($\frac{k_3}{VnF}$): 0.71×10^{-3} and $0.97 \times 10^{-3}\ \text{s}^{-1}$, is remarkable considering that the values were determined by unrelated methods and the simplicity of the model employed. This indicates that the principles and assumptions upon which the model is based are broadly correct.

Conclusions

Studies of the oxidation of hydrogen in a SOFC with molten tin anode were carried out. The anode was operated at -0.90 V versus an air RE, which is within an 'inert' potential window. Steady anodic currents were essentially proportional to hydrogen partial pressure and independent of total gas flow rate. Two models were considered for either (i) direct anodic oxidation of dissolved hydrogen or (ii) homogeneous reaction between dissolved hydrogen and oxygen followed by anodic injection of oxygen to replace that removed by the chemical reaction. The former model was rejected as it required the incorporation of the hydrogen/ argon fuel gas in the form of a persistent foam which was not detected. Oxygen solubility values are compatible with the latter model which was validated using steady-state and dynamic experimentally-generated data.

The development of the theoretical framework has generated the parameter $\bar{z}$. This parameter does not have fundamental significance but is of technological importance when designing LMA SOFC reactors. Theory shows that $\bar{z}$ depends upon geometric factors (including the volume of tin), applied potential and diffusion layer thickness (and hence degree of convection); its value is required in order to obtain a fuller understanding of experimentally-generated results.

This study has clarified the behavior of the oxygen-hydrogen-tin system in the 'inert window' and provides a firm basis for proceeding with studies via the Rotating Electrolyte Disc (RED).

Acknowledgments

List of Symbols

Parameters and Variables	Description
a	Rate of electrochemical oxidation of metal to metal oxide
b	Rate of chemical reduction of metal oxide to metal
c'	Concentration of hydrogen in the bulk of the melt/mol cm^{-3}
$\bar{c}$	Concentration of dissolved oxygen in the bulk of the melt/mol cm^{-3}
$\bar{c}^*$	Saturated concentration of oxygen at potential E in the bulk of the melt at $p' = 0$/mol cm^{-3}
$\bar{c}_1$	Steady concentration of oxygen in the bulk of the melt at p'_1/mol cm^{-3}
$\bar{c}_2$	Steady concentration of oxygen in the bulk of the melt at p'_2/mol cm^{-3}
$\bar{D}$	Diffusion coefficient of oxygen in the melt/cm^2 s^{-1}
E	Potential/V
F	Faraday constant/96,485 C mol-eq^{-1}
i	Anodic oxidation current/mA
i_1	Steady anodic current at p'_1/ mA
i_2	Steady anodic current at p'_2/mA
$\bar{J}$	Flux of oxygen in the melt /mol s^{-1}
k_1	Rate constant for homogeneous oxidation of hydrogen in liquid metal/s^{-1} (mol cm^{-3})$^{-2}$
k_2	Equilibrium constant for hydrogen dissolution in liquid metal/mol cm^{-3} kPa$^{-0.5}$
k_3	Proportionality constant in Equation 13/C cm^3 (mol-eq^{-1} s)$^{-1}$
$\bar{K}$	Sub-parameter of $\bar{z}_2$, defined by Equations 31 and 32 and dependent upon geometric and convective factors
n	Number of electrons transferred in Reaction 2
n	Stoichiometric number
$\bar{N}$	Number of moles of oxygen
p'	Partial pressure of hydrogen/kPa
p'_1	Partial pressure of hydrogen at $t = 0$/kPa
p'_2	Partial pressure of hydrogen at $t = t_1$/kPa
s_1	Slope of $[\frac{di}{dt}]_{t=t_1}$ vs. p'_2 equivalent to $k_1(k_2)^2 k_3 \bar{c}^*$
s_2	Slope of i_2 vs. $\bar{z}_2\,p'_2$ equivalent to $nFVk_1(k_2)^2\bar{c}^*$
t	Time/s
t_1	Time at which $p(H_2)$ changes from p'_1 to p'_2/s
V	Volume of the melt (liquid tin)/cm^3
$\bar{z}$	New parameter taking a value between zero and unity, given by Equation 17; it influences the current via Equation 30
x	Ratio of the two rates: electrochemical oxidation of metal to metal oxide and chemical reduction of metal oxide to metal

Greek

δ	Diffusion layer thickness/cm

Subscripts

n	stoichiometric number
l	liquid

Superscripts

'	hydrogen
-	oxygen

References

1. T. Tao, M. Slaney, L. Bateman, and J. Bentley, *ECS Trans.*, **7**, 1389 (2007).
2. T. Tao, L. Bateman, J. Bentley, and M. Slaney, *ECS Trans.*, **5**, 463 (2007).
3. A. Jayakumar, J. M. Vohs, and R. J. Gorte, *Ind. Eng. Chem. Res.*, **49**, 10237 (2010).
4. A. Jayakumar, R. Küngas, S. Roy, A. Javadekar, D. J. Buttrey, J. M. Vohs, and R. J. Gorte, *Energy Environ. Sci.*, **4**, 4133 (2011).
5. M. LaBarbera, M. Fedkin, and S. Lvov, *ECS Trans.*, **35**, 2725 (2011).
6. A. Jayakumar, S. Lee, A. Hornés, J. M. Vohs, and R. J. Gorte, *J. Electrochem. Soc.*, **157**, B365 (2010).
7. A. Javadekar, A. Jayakumar, R. J. Gorte, J. M. Vohs, and D. J. Buttrey, *J. Electrochem. Soc.*, **159**, A386 (2012).
8. W. A. G. McPhee, M. Boucher, J. Stuart, R. S. Parnas, M. Koslowske, T. Tao, and B. A. Wilhite, *Energy & Fuels*, **23**, 5036 (2009).
9. M. Colet Lagrille, U. Doraswami, and G. H. Kelsall, *ECS Trans.*, **41**, 137 (2012).
10. H. Wang, Y. Shi, and N. Cai, *J. Power Sources*, **245**, 164 (2014).

11. T. T. Tao, M. T. Koslowske, J. Bentley, J. Brodie, and C. MacKean, *ECS Trans.*, **41**, 125 (2012).
12. T. Tao, W. A. McPhee, M. T. Koslowske, L. S. Bateman, M. J. Slaney, and J. Bentley, *ECS Trans.*, **12**, 681 (2008).
13. T. Cao, H. Wang, Y. Shi, and N. Cai, *Fuel*, **135**, 223 (2014).
14. H. Wang, Y. Shi, W. Yuan, T. Cao, N. Cai, and X. Liang, *ECS Trans.*, **57**, 2913 (2013).
15. H. Abernathy, R. Gemmen, K. Gerdes, M. Koslowske, and T. Tao, *J. Power Sources*, **196**, 4564 (2011).
16. R. Gemmen, H. Abernathy, K. Gerdes, M. Koslowske, W. A. G. McPhee, and T. Tao, in *Advances in Solid Oxide Fuel Cells V*, N. P. Bansal and P. Singh, Editors, p. 37, John Wiley & Sons, New Jersey (2009).
17. A. Toleuova, V. Yufit, S. Simons, W. C. Maskell, and D. J. L. Brett, *J. Electrochem. Sci. Eng*, **3**, 91 (2013).
18. T. Tao, in *Solid Oxide Fuel Cells IX*, S. C. Singhal and J. Mizusaki, Editors, p. 353, The Electrochemical Society, Pennington, N. J. (2005).
19. A. D. Javadekar, thesis, University of Delaware (2012).
20. S. Khurana, M. LaBarbera, M. V. Fedkin, S. N. Lvov, H. Abernathy, and K. Gerdes, *J. Power Sources*, **274**, 1049 (2015).
21. H. Wang, Y. Shi, and N. Cai, *J. Power Sources*, **246**, 204 (2014).
22. T. A. Ramanarayanan and R. A. Rapp, *Metall. Trans.*, **3**, 3239 (1972).
23. K. T. Jacob, *ECS Trans.*, **35**, 573 (2011).
24. I. Barin, *Thermochemical Data of Pure Substances*, VCH VerlagsgesellschaftmbH, Weinheim, (1995).
25. A. Toleuova, V. Yufit, S. J. R. Simons, W. C. Maskell, and D. J. L. Brett, *ECS Trans.*, **58**, 65 (2013).
26. W. C. Maskell and B. C. H. Steele, *J. Appl. Electrochem.*, **16**, 475 (1986).
27. S. B. Adler, *J. Electrochem. Soc.*, **149**, E166 (2002).
28. G. Offer, D. Brett, and N. Brandon, *ECS Trans.*, **7**, 1645 (2007).
29. M. A. Colet Lagrille, thesis, Imperial College London (2013).
30. J. Winkler, P. V. Hendriksen, N. Bonanos, and M. Mogensen, *J. Electrochem. Soc.*, **145**, 1184 (1998).
31. G. Jiang, Y. Li, and Y. Liu, *Trans. Nonferrous Met. Soc. China*, **21**, 1130 (2011).
32. C. Wagner, *Thermodynamics of alloys*, Addison-Wesley Press, (1952).
33. H. M. Lee, *Metall. Trans. A*, **7A**, 431 (1976).
34. T. Gnanasekaran, *J. Nucl. Mater.*, **274**, 252 (1999).
35. S. Pati, K. J. Yoon, S. Gopalan, and U. B. Pal, *J. Electrochem. Soc.*, **156**, B1067 (2009).